

Impacts of Hurricane Irma (2017) on ocean transport processes

Thomas Dobbelaere^{a,*}, Milan Curcic^b, Matthieu le Hénaff^{c,d}, Emmanuel Hanert^{a,e}

^a*Eath and Life Institute (ELI), UCLouvain, Louvain-la-Neuve, Belgium*

^b*Rosenstiel School of Marine and Atmospheric Sciences (RSMAS), University of Miami, Coral Gables, Florida, USA*

^c*Cooperative Institute for Marine and Atmospheric Studies (CIMAS), University of Miami, Miami, Florida, USA*

^d*Atlantic Oceanographic and Meteorological Laboratory (AOML), NOAA, Miami, Florida, USA*

^e*Institute of Mechanics, Materials and Civil Engineering (IMMC), UCLouvain, Louvain-la-Neuve, Belgium*

Abstract

Tropical cyclones are becoming more intense and more frequent. Their effect is particularly acute in coastal areas where they cause extensive damage leading to an influx of debris, sediments and waste to the sea. However, most coastal ocean models do not represent heavy-wind transport processes correctly as they do not couple the hydrodynamics with the wind-generated waves. This may lead to significant errors during a tropical cyclone. Here, we investigate current-wave interactions during a major hurricane and assess their impact on transport processes. We do that by coupling the unstructured-mesh coastal ocean model SLIM with the spectral wave model SWAN, and applying it to the Florida Reef Tract during Hurricane Irma (Sept. 17). We show that the coupled model successfully reproduces the wave behavior, the storm surge and the ocean currents during the passage of the hurricane. We then use the coupled and uncoupled wave-current model to simulate the transport of

*Corresponding author

Email address: thomas.dobbelaere@uclouvain.be (Thomas Dobbelaere)

passive drifters. We show that the wave radiation stress gradient alone can lead to changes of up to 1 m/s in the modeled currents, which in turn leads to differences of up to 5 km in the position of drifting material over the duration of the hurricane. The Stokes drift appears however appears to be up to 4 times more intense and should thus be considered in priority. Wave-current interactions therefore strongly impact the transport of drifting material such as sediments and debris in the aftermath of a hurricane. They should thus be taken into account in order to correctly assess its overall impact.

Keywords:

1. Introduction

2 Tropical cyclones are becoming more intense and more frequent (Bhatia
3 et al., 2019; Kossin et al., 2020). This increase is likely due to climate change
4 and will probably continue in the future (Knutson et al., 2020). However,
5 estimating the impact of tropical cyclones on the coastal ocean circulation
6 remains a challenge. Understanding wave-current interactions and being able
7 to represent their impact on coastal ocean transport processes is central to
8 many coastal activities such as dredging, erosion management, O&G, search
9 and rescue and insurance (Bever and MacWilliams, 2013; Li and Johns, 1998;
10 Breivik et al., 2013). All these activities require wave-current models to
11 predict the impact of tropical cyclones on the coastal circulation and on
12 water-level changes.

13 Wave-current interactions during a cyclone are highly nonlinear and can
14 vary significantly in space and time (Wu et al., 2011). Wave-induced currents
15 are generated by wave radiation stress gradients (Longuet-Higgins, 1970),
16 affecting water levels near shorelines and wave breaking points (Longuet-
17 Higgins and Stewart, 1964). Changes in water levels and currents, in turn,
18 affect the motion and evolution of the waves (Sikirić et al., 2013). Coupled
19 wave-current models hence require the calculation of the full two-dimensional
20 wave spectrum in order to correctly reproduce the dynamics of wind-driven

21 surface waves. This is usually achieved by considering spectral wave models,
22 which describe the evolution of the wave energy spectrum. As of today,
23 the most popular spectral wave models are WAM (WAMDI Group, 1988),
24 TOMAWAC (Benoit et al., 1997), SWAN (Booij et al., 1999), and WAVE-
25 WATCH III (Tolman et al., 2009). Among these models, SWAN is more
26 fitted to coastal applications, as it represents depth-induced wave breaking
27 and triad wave-wave interactions, while implementing numerical techniques
28 adapted to small-scale, shallow water regions (Booij et al., 1999).

29 Coastal oceans are characterized by the complex topography of the coast-
30 line and the presence of islands, reefs and artificial structures. Traditional
31 structured-grid models often lack the flexibility to simulate near-shore pro-
32 cesses at a sufficiently small scale. Instead, unstructured-mesh models can
33 easily adapt to the topography and are hence better suited to coastal processes
34 (Fringer et al., 2019). Being able to capture the impact of the topography
35 on wave interactions becomes even more important in the case of tropical cy-
36 clones. Heavy winds generate large wind-waves and disturb ocean conditions
37 (Liu et al., 2020) by causing coastal upwellings on continental shelves (Smith,
38 1982) and inducing strong currents, waves and storm surges in nearshore and
39 coastal regions (Dietrich et al., 2010; Weisberg and Zheng, 2006).

40 The transport of drifting objects or substances that are locally released
41 is often best represented by a Lagrangian individual-based model. Such
42 an approach is routinely used to model the dispersal of larvae, pollutants,
43 sediments and many other tracers (e.g. Le Hénaff et al., 2012; Liubartseva
44 et al., 2018; Figueiredo et al., 2013; Frys et al., 2020). Although some transport
45 models take the impact of waves into account by adding a Stokes drift velocity,
46 *i.e.* the net drift of a floating particle in the direction of the wave propagation
47 (Van Den Bremer and Breivik, 2018), to the Eulerian currents, they usually
48 neglect the wave-induced currents. Such practice is reasonable in the case
49 of fair weather, when wave-induced forces exerted on currents are relatively
50 small, but might lead to significant errors during storm conditions (Röhrs

51 et al., 2012; Curcic et al., 2016).

52 The objective of this study is therefore to assess the importance of wave-
53 current interactions during a tropical cyclone. We investigate the transport
54 of drifting particles on the Florida shelf during Hurricane Irma, one of the
55 strongest and costliest tropical cyclones on record in the Atlantic Basin
56 (Xian et al., 2018), which made landfall in Florida in September 2017. To
57 do that, we developed an unstructured-mesh coupled wave-current model
58 of South Florida to simulate the ocean circulation during hurricane Irma.
59 Both modeled currents and waves were validated against field measurements
60 and then used to simulate the transport of drifting material in the Florida
61 Keys and the Florida inner shelf. Model outputs were then compared with
62 uncoupled simulation results in order to assess the impact of wave-induced
63 forces and Stokes drift on the modeled currents and transports.

64 **2. Methods**

65 *2.1. Study area and observational data*

66 The large-scale ocean circulation around South Florida is dominated by
67 the Florida Current (FC), which originates from the Loop Current (LC) where
68 it enters the Florida Straits from the Gulf of Mexico, and, downstream, forms
69 the Gulf Stream. The FC is a major western boundary current characterized
70 by spatial variability and meandering, associated with the presence of cyclonic
71 eddies between the core of the current and the complex reef topography
72 of the Florida Reef Tract (FRT) (Lee et al., 1995; Kourafalou and Kang,
73 2012). The variability of the FC extends over a large range of spatial and
74 temporal scales, with periods of 30-70 days in the Lower Keys (Lee et al., 1995)
75 and shorter periods of 2-21 days in the Upper Keys (Lee and Mayer, 1977),
76 and exhibits significant seasonal and interannual cycles (Johns and Schott,
77 1987; Lee and Williams, 1988; Schott et al., 1988). Circulation on the West
78 Florida Shelf (WFS), on the other hand, is forced by local winds and tidal
79 fluctuations (Lee and Smith, 2002; Liu and Weisberg, 2012). Furthermore,

80 due to its location relative to the warm waters of the North Atlantic, Florida
81 is particularly vulnerable to tropical cyclones. On average, the state gets
82 hit by a hurricane every two years and strong hurricanes, some of which are
83 among the most destructive on record, strike Florida on average once every
84 four years (Malmstadt et al., 2009).

85 The state of the ocean around Florida is monitored by an extensive
86 array of tide gauges, current meters and buoys. In this study, we used sea
87 surface elevation measurements from the National Oceanic and Atmospheric
88 Administrations (NOAA) Tides and Currents dataset. These measurements
89 were taken at four locations: two in the Florida Keys (Key West and Vaca Key);
90 one on the eastern coast of Florida (Virginia Key); and one on the western
91 coast (Naples). For the currents, we used ADCP measurements from the
92 University of South Florida's College of Marine Science's (USF/CMS) Coastal
93 Ocean Monitoring and Prediction System (COMPS) for the WFS (Weisberg
94 et al., 2009). More specifically, we used measurements from moorings C10,
95 C12 and C13, respectively located at the 25, 50, and 50 m isobaths of the
96 WFS (Liu et al., 2020). Finally, for the waves, we used measurements from
97 four buoys of the NOAA's National Data Buoy Center (NDBC); two on
98 Florida's eastern shelf and two on the WFS. The locations of all measurement
99 stations are shown in Fig. 1A,C.

100 *2.2. Wind and atmospheric pressure during Hurricane Irma*

101 Hurricane Irma made landfall in Florida on 10 September 2017 as a
102 category 3 hurricane, first at Cudjoe Key (Florida Keys) and later on Marco
103 Island, south to Naples (see hurricane track in Fig. 1). It then weakened to a
104 category 2 hurricane as it moved further inland (Pinelli et al., 2018). The
105 storm damaged up to 75% of the buildings at its landfall point in the Florida
106 Keys, making it one of the strongest and costliest hurricanes on record in the
107 Atlantic basin (Xian et al., 2018; Zhang et al., 2019). The strongest reported
108 wind speed was 50 m/s on Marco Island while the highest recorded storm
109 surge was 2.3 m, although larger wind speed likely occurred in the Florida

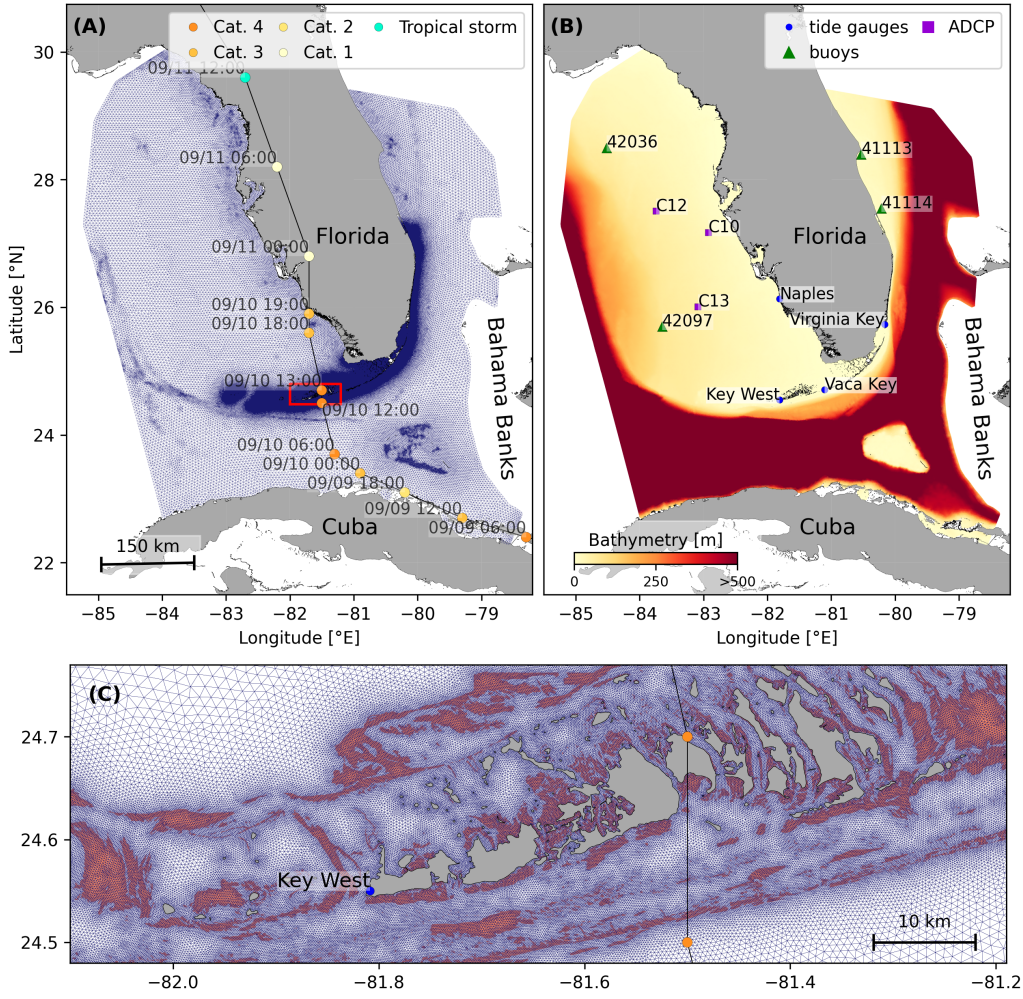


Fig. 1: (A) Mesh of the computational domain with the trajectory of Irma. The category of the hurricane is given by the Saffir-Simpson color scale. (B) Bathymetry of the domain with the location of stations used for the validation of the model outputs. (C) Close up view of the Lower Keys area, where the mesh resolution reaches 100m near reefs (shown in dark orange) and islands (highlighted in dark grey)

110 Keys (Pinelli et al., 2018). In order to reproduce the wind profile of Irma in
111 our model, we used high-resolution H*Wind wind fields (Powell et al., 1998).
112 As these data represent 1-min averaged wind speeds, we multiplied them by a
113 factor 0.93 to obtain 10-min averaged wind speeds (Harper et al., 2010), which
114 are more consistent with the time step of our model. Furthermore, H*Wind
115 wind profiles did not cover the whole model extent during the passage of the
116 hurricane and were thus blended within coarser wind field extracted from
117 ECMWF ERA-5 datasets (Fig. 2A). The pressure field during the passage
118 of Hurricane Irma was also reconstructed using ERA-5 data. However, the
119 coarse resolution of the dataset smoothes out the depression at the center of
120 the hurricane, leading to an underestimation of the pressure gradient (Fig.
121 2B). To better capture the central depression of Irma, we therefore built a
122 hybrid pressure field using the position and the minimal pressure of the core
123 of the hurricane based on its track as recorded in the HURDAT 2 database
124 (Landsea and Franklin, 2013). Based on this information, the hybrid pressure
125 field was constructed by combining an idealized Holland pressure profile (Lin
126 and Chavas, 2012) within the radius of maximum wind speed of Irma (Knaff
127 et al., 2018) with ERA-5 pressure field. The transition from the Holland
128 profile to ERA-5 data outside the radius of maximum wind speed data was
129 performed using a smooth step function (Fig. 2).

130 *2.3. Hydrodynamic model*

131 Ocean currents generated during hurricane Irma around South Florida
132 were modeled using the 2D barotropic version of the unstructured-mesh
133 coastal ocean model SLIM¹ (Lambrechts et al., 2008). The model mesh covers
134 an area similar to the model extent of Dobbelaere et al. (2020), that includes
135 the FRT but also the Florida Straits and part of the Gulf of Mexico (Figure 1).
136 However, this area has been slightly extended northeastward and westward
137 in order to include the NOAA-NDBC buoys. Furthermore, to withstand

¹<https://www.slim-ocean.be>

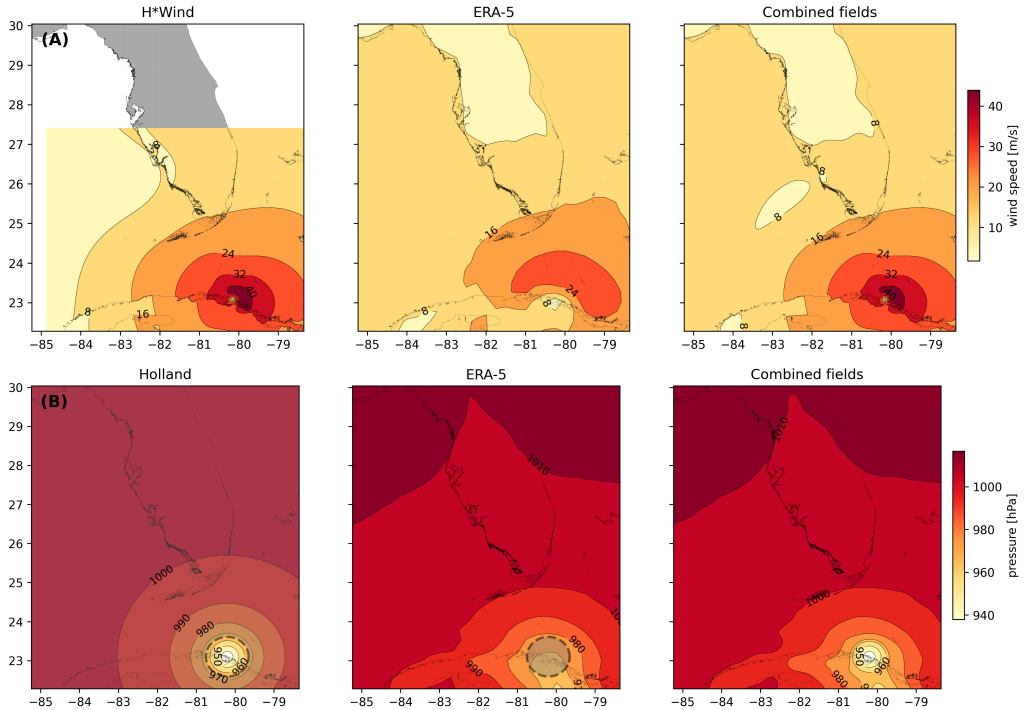


Fig. 2: Snapshot of the hybrid wind (A) and pressure (B) profiles constructed to capture the passage of Hurricane Irma at 1800 UTC on 9 September 2017. Wind profiles are obtained by combining high resolution H*Wind with coarser ERA-5 wind fields. The pressure field is built by combining the ERA-5 pressure field with an idealized Holland pressure profile based on the track of Irma in the HURDAT 2 database. Holland field was only used within the radius of maximum wind speed (dashed grey line) of the hurricane to capture its central depression.

¹³⁸ potential cell drying during the hurricane, we solved the conservative shallow
¹³⁹ water equations with wetting-drying:

$$\begin{aligned} \frac{\partial H}{\partial t} + \nabla \cdot (\mathbf{U}) &= 0 , \\ \frac{\partial \mathbf{U}}{\partial t} + \nabla \cdot \left(\frac{\mathbf{U}\mathbf{U}}{H} \right) + f\mathbf{e}_z \times \mathbf{U} &= \alpha g H \nabla(H - h) - \frac{1}{\rho} \nabla p_{\text{atm}} + \frac{1}{\rho} \boldsymbol{\tau}_s \\ &\quad + \nabla \cdot (\nu \nabla \mathbf{U}) - \frac{C_b}{H^2} |\mathbf{U}| \mathbf{U} + \gamma (\mathbf{U}_{\text{ref}} - \mathbf{U}) , \end{aligned} \quad (1)$$

¹⁴⁰ where H is the water column height and \mathbf{U} is the depth-averaged transport;
¹⁴¹ f is the Coriolis coefficient; g is the gravitational acceleration; h is the
¹⁴² bathymetry; α is a coefficient indicating whether the mesh element is wet
¹⁴³ ($\alpha = 1$) or dry ($\alpha = 0$) (Le et al., 2020); ν is the viscosity; C_b is the
¹⁴⁴ bulk bottom drag coefficient; p_{atm} is the atmospheric pressure; $\boldsymbol{\tau}_s$ is the
¹⁴⁵ surface stress, usually due to wind; and γ is a relaxation coefficient towards a
¹⁴⁶ reference transport \mathbf{U}_{ref} . As in Frys et al. (2020) and Dobbelaere et al. (2020),
¹⁴⁷ SLIM currents were gradually relaxed towards the operational Navy HYCOM
¹⁴⁸ product (GOMl0.04², Chassignet et al. (2007)) in regions where the water
¹⁴⁹ depth exceeds 50m.

¹⁵⁰ At very high wind speeds, the white cap is blown off the crest of the
¹⁵¹ waves. This phenomenon, also known as spumes, has been hypothesized to
¹⁵² generate a layer of droplets that acts as a slip layer for the winds at the
¹⁵³ ocean-atmosphere interface (Holthuijsen et al., 2012). It causes a saturation
¹⁵⁴ of the wind drag coefficient for strong winds (Powell et al., 2003; Donelan
¹⁵⁵ et al., 2004; Curcic and Haus, 2020). We take this saturation effect into
¹⁵⁶ account by using the wind drag parameterization of Moon et al. (2007). In
¹⁵⁷ this parameterization, the drag coefficient C_d depends on the wind speed at

²<https://www.hycom.org/data/goml0pt04>

₁₅₈ 10-m height U_{10} according to:

$$C_d = \kappa^2 \log \left(\frac{10}{z_0} \right)^{-2} \quad (2)$$

₁₅₉ where κ is the von Karman constant and z_0 is the roughness length expressed
₁₆₀ as:

$$z_0 = \begin{cases} \frac{0.0185}{g} U_*^2 & \text{if } U_{10} \leq 12.5 \text{ m/s ,} \\ [0.085(-0.56U_*^2 + 20.255U_* + 2.458) - 0.58] \times 10^{-3} & \text{if } U_{10} > 12.5 \text{ m/s ,} \end{cases} \quad (3)$$

₁₆₁ with U_* the friction velocity. The relation between U_{10} and U_* is given by:

$$U_{10} = -0.56U_*^2 + 20.255U_* + 2.458 . \quad (4)$$

₁₆₂ The mesh resolution depends on the distance to the coastlines and reefs
₁₆₃ following the approach of Dobbelaere et al. (2020). The mesh is then further
₁₆₄ refined according to bathymetry value and gradient, as suggested in the
₁₆₅ SWAN user-guide³. Such an approach improves the model efficiency as the
₁₆₆ mesh resolution is only increased where required by the currents and waves
₁₆₇ dynamics. The mesh was generated with the seamsh⁴ Python library, which is
₁₆₈ based on the open-source mesh generator GMSH (Geuzaine and Remacle,
₁₆₉ 2009). It is composed of approximately 7.7×10^5 elements. The coarsest
₁₇₀ elements, far away from the FRT, has a characteristic length of about 5 km
₁₇₁ whereas the finest elements have a characteristic length of about 100 m along
₁₇₂ the coastlines and over the reefs (Fig 1).

₁₇₃ *2.4. Wave model*

₁₇₄ Waves were modeled using the parallel unstructured-mesh version of the
₁₇₅ Simulating WAves Nearshore (SWAN) model (Booij et al., 1999), one of the

³<http://swanmodel.sourceforge.net/unswan/unswan.htm>

⁴<https://pypi.org/project/seamsh/>

176 most popular wave models for coastal areas and inland waters. It solves the
177 action balance equation (Mei, 1989):

$$\frac{\partial N}{\partial t} + \nabla_{\mathbf{x}} \cdot [(\mathbf{c}_g + \mathbf{u})N] + \frac{\partial}{\partial \theta}[c_\theta N] + \frac{\partial}{\partial \sigma}[c_\sigma N] = \frac{S_{in} + S_{ds} + S_{nl}}{\sigma}, \quad (5)$$

178 where $N = E/\sigma$ is the wave action density and E is the wave energy spectrum;
179 θ is the wave propagation direction; σ is the intrinsic wave frequency; \mathbf{c}_g is the
180 wave group velocity, $\mathbf{u} = \mathbf{U}/H$ is SLIM depth-averaged current velocity; c_θ
181 and c_σ are the propagation velocities in spectral space due to refraction and
182 shifting in frequency due to variations in depth and currents; and S_{in} , S_{ds} ,
183 and S_{nl} respectively represent wave growth by wind, wave decay and nonlinear
184 transfers of wave energy through interactions between triplets and quadruplets.
185 The wave spectra were discretized with 48 direction bins and 50 frequency
186 bins logarithmically distributed from 0.03 to 2 Hz. Exponential wind growth
187 was parameterized using the formulation of Janssen (1991), while dissipations
188 by whitecapping and bottom dissipations followed the formulations of Komen
189 et al. (1984) and Madsen et al. (1989), respectively.

190 Coefficients for exponential wind growth and whitecapping parameteriza-
191 tions were based on the results of Siadatmousavi et al. (2011), and significantly
192 differ from SWAN's default settings. By default, SWAN implements the wind
193 input formulation of Komen et al. (1984) and the steepness-dependent coeffi-
194 cient governing dissipation by whitecapping is a linear function of the wave
195 number. In this study, this steepness-dependent coefficient is a quadratic
196 function of the wave number, as it showed better predictions of the significant
197 wave height in the study of Siadatmousavi et al. (2011). The choice of these
198 formulations was motivated by the appearance of numerical instabilities in
199 the region of the Gulf Stream when using SWAN's default parameter values.
200 Finally, wave boundary conditions were derived from WAVEWATCH III
201 (Tolman et al., 2009) spectral outputs at NDBC buoy locations. We selected
202 these datasets as the large number of NDBC buoys around our region of
203 interest allowed for a fine representation of the wave spectra on the boundary

204 of the domain.

205 Surface waves induce a net drift in the direction of the wave propagation,
206 known as the Stokes drift (Van Den Bremer and Breivik, 2018; Stokes,
207 1880). This net drift has a significant impact on sediment transport in
208 nearshore regions (Hoefel and Elgar, 2003), on the formation of Langmuir
209 cells (Langmuir, 1938; Craik and Leibovich, 1976) as well as on the transport
210 of heat, salt or pollutants such as oil or micro-plastic in the upper ocean layer
211 (McWilliams and Sullivan, 2000; Röhrs et al., 2012; Drivdal et al., 2014). To
212 correctly model the Stokes drift profile in mixed wind-driven sea and swell
213 conditions, the full two-dimensional wave spectrum must be represented by a
214 spectral wave model within a wave-current coupling (Van Den Bremer and
215 Breivik, 2018). We therefore used SWAN modeled spectra to compute the
216 Stokes drift as follows:

$$\mathbf{u}_s = \int_0^{2\pi} \int_0^{+\infty} \frac{\sigma^3}{h \tanh(2kh)} E(\sigma, \theta) (\cos \theta, \sin \theta) d\sigma d\theta , \quad (6)$$

217 where k is the norm of the wave vector; h is the water depth; and $E(\sigma, \theta)$ is
218 the wave energy density.

219 2.5. Coupled model

220 SLIM and SWAN are coupled so that they run on the same computational
221 core and the same unstructured mesh. SLIM is run first and passes the
222 wind velocity (\mathbf{U}_{10}), water level ($\eta = H - h$) and depth-averaged current
223 ($\mathbf{u} = \mathbf{U}/H$) fields to SWAN, as well as a roughness length (z_0) for the bottom
224 dissipation formulation of Madsen et al. (1989). This roughness length is
225 computed from SLIM's bulk drag coefficient C_b following the approach of
226 Dietrich et al. (2011) so that both models have consistent bottom dissipation
227 parameterizations. SWAN then uses these quantities to compute the wave
228 radiation stress gradient, that is then passed to SLIM as the force exerted
229 by waves on currents $\boldsymbol{\tau}_{\text{wave}}$ (Fig. 3). SLIM then uses this quantity to
230 update the value of the surface stress $\boldsymbol{\tau}_s$ in Eq. (1), that now becomes

231 the sum of wind and wave-induced stresses $\tau_s = \tau_{\text{wind}} + \tau_{\text{wave}}$. Here, the
232 momentum flux from the atmosphere to the ocean is taken as the commonly-
233 used full wind stress τ_{wind} . Doing so, we neglect the momentum advected
234 away from the storm by the waves, leading to a 10-15% overestimation of the
235 momentum flux in hurricane winds (Curcic, 2015). Moreover, we followed
236 the approach of Dietrich et al. (2012) by characterizing the wave-induced
237 stresses using the radiation-stress representation instead of the vortex-force
238 representation (McWilliams et al., 2004). Although the latter provides a clearer
239 and more meaningful decomposition of the wave effect, we implemented the
240 first representation for the sake of simplicity as it allows us to provide the
241 whole wave contribution as an additional surface stress to SLIM (Lane et al.,
242 2007).

243 SLIM's governing equations are integrated using an implicit time inte-
244 gration scheme while SWAN is unconditionally stable (Dietrich et al., 2012),
245 allowing both models to be run with relatively large time steps. In this study,
246 the stationary version of SWAN was used, *i.e.* the time derivative of Eq. (5)
247 was set to zero. This resulted in reduced scaling and convergence rates than
248 with the nonstationary version of SWAN but increased the stability of the
249 model. The wave spectra at each node of the mesh was saved at the end of
250 each iteration to serve as initial conditions for the next one. Both models
251 were run sequentially using a time step of 600 s, so that each computational
252 core was alternatively running either SLIM or SWAN. As in the coupling
253 between SWAN and ADCIRC (Dietrich et al., 2012), both models use the
254 same local sub-mesh, allowing for a one-to-one correspondence between the
255 geographic locations of the mesh vertices. No interpolation is therefore needed
256 when passing the discretised variables from one model to the other, which
257 allows an efficient inter-model communication. However, as SLIM is based on
258 a discontinuous Galerkin finite element method, an additional conversion step
259 to a continuous framework was required to transfer SLIM nodal quantities to
260 SWAN.

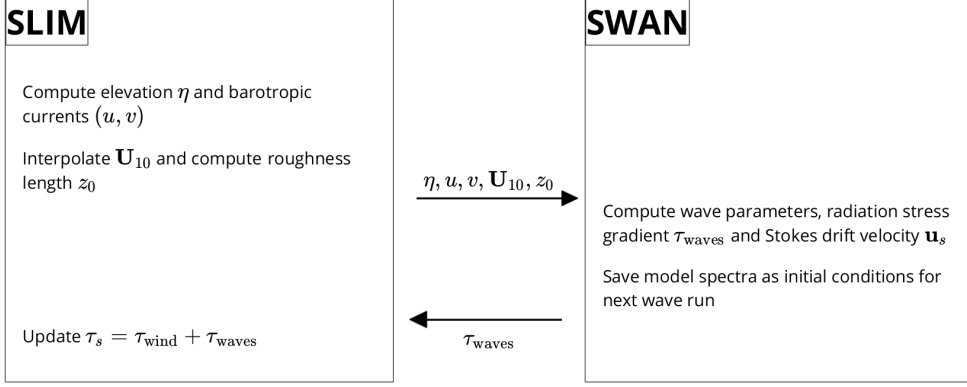


Fig. 3: Schematic illustration of the coupled SLIM+SWAN model.

261 *2.6. Quantifying the effect of wave-current interactions on transport*

262 To quantify the impact of wave-current interactions on transport processes,
 263 we compared the trajectories of passive particles advected by the uncoupled
 264 SLIM and coupled SLIM+SWAN currents during the passage of Irma in the
 265 Lower Keys. Furthermore, the depth-averaged Stokes drift was computed
 266 using the wave spectra of the coupled model SLIM+SWAN run as well as
 267 those of an uncoupled SWAN run. Particles were released on the inner and
 268 outer shelves at the points highlighted by red and blue dots in Fig. 4 on
 269 Sept. 7 at 0000 UTC and then tracked until Sept. 15. These initial particle
 270 positions were found using backtracking methods (Spivakovskaya et al., 2005)
 271 to ensure that the release particles would intersect the path of Irma during
 272 its passage through the Florida Keys. We first defined two 25 km² circular
 273 regions on the trajectory of the hurricane (see red and blue circles in Fig. 4).
 274 Particles within these two regions were then tracked backward in time using
 275 uncoupled SLIM currents from the exact time of the passage of the hurricane
 276 until Sept. 7 at 0000 UTC. Their positions at the end of the backward
 277 simulation (see red and blue particle clouds in Fig. 4) corresponds to the
 278 initial condition of the forward transport simulations described below. We
 279 then compared the trajectories of particles originating from these regions and

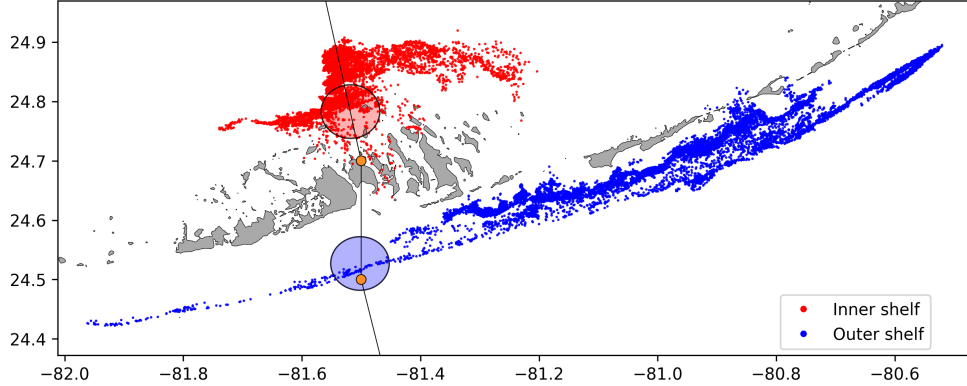


Fig. 4: Release regions of the passive particles on the inner and outer shelves (red and blue clouds) obtained by backtracking particles released in the red and blue circular areas during the passage of Irma.

advedted forward in time by different sets of currents: (i) uncoupled SLIM currents alone; (ii) coupled SLIM+SWAN currents; (iii) SLIM currents with the addition of the depth-averaged Stokes drift computed with the coupled wave-current model (Stokes-C); (iv) SLIM+SWAN currents with Stokes-C; and (v) SLIM currents with the depth-averaged Stokes drift computed with the uncoupled wave model (Stokes-U). Particles trajectories are compared by computing the distances between the centers of mass of the particle clouds through time.

3. Results

We first validated the reconstructed atmospheric fields of hurricane Irma as well as the outputs of our coupled wave-current model against field measurements. We then used the validated model outputs to simulate the transport of passive drifters in the Lower Keys during the passage of Hurricane Irma. These drifters were advected by the sets of currents described in section 2.6 and their trajectories were compared to evaluate the impact of the wave-current interactions and the Stokes drift on the transport processes during the passage of Irma.

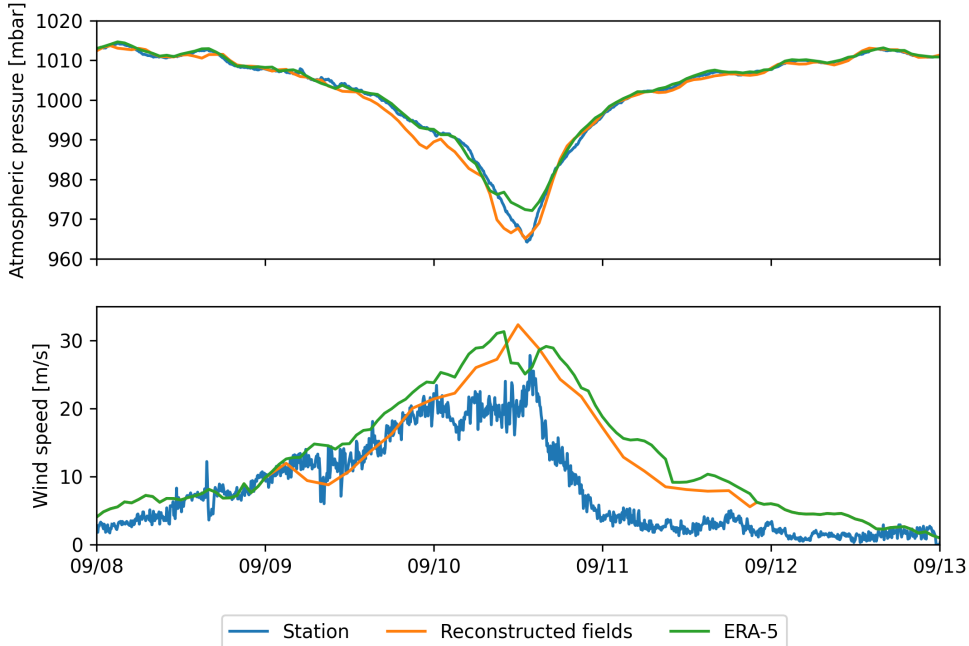


Fig. 5: Comparison of reconstructed wind atmospheric pressure with field measurements and coarser ECMWF ERA-5 profiles at Vaca Key station. The generated hybrid atmospheric forcings better reproduce the observed storm depression while H*wind winds better reproduce the measured peak in wind speed.

297 3.1. *Model validation*

298 H*Wind winds and hybrid pressure field agree well with station mea-
 299 surements at Vaca Key station (Fig. 5). The hybrid pressure field shows a
 300 better agreement with observations than ERA-5 pressure as it successfully
 301 reproduces the storm depression. ERA-5 fields, on the other hand, fail to
 302 reproduce the low pressure at the core of the hurricane due to their coarser
 303 grid, leading to an overestimation of 8 mbar of the storm depression. Both
 304 H*Wind and ERA-5 agree well with observed wind speeds although both
 305 data sets tend to slightly overestimate the width and intensity of the wind
 306 peak. However, H*wind profiles better reproduce the timing of the observed
 307 peak, as ERA-5 winds tend to anticipate it. H*wind also exhibits a slightly
 308 narrower peak in wind speed, which better agrees with observations.

309 Hydrodynamic outputs of the coupled wave-current model agree well with
310 tide gauge (Fig. 6) and ADCP measurements (Fig. 7). Despite a slight
311 overestimation of the amplitude of sea surface elevation (Table 1) in fair
312 weather conditions, the timing and amplitude of the storm surges are well
313 reproduced by the coupled model. The largest model error during the surge
314 is an overestimation of 18 cm of the elevation peak at Virginia Key. The fit is
315 especially good at Naples, where both the large positive and negative surges
316 are captured by the coupled model with an error of less than 5 cm. modeled
317 2D currents were validated against depth-averaged ADCP measurements
318 at mooring stations C10, C12 and C13 (Fig. 7). As in Liu et al. (2020),
319 we performed the vector correlation analysis of Kundu (1976) to compare
320 modeled and observed current velocity vectors. Correlation coefficients (ρ)
321 between simulated and observed depth-averaged currents are 0.84, 0.74 and
322 0.73 at stations C10, C12 and C13, respectively. The average veering angles
323 are below 12°, as in (Liu et al., 2020). Furthermore, the positive bias in Table
324 1 indicates that our model tends to underestimate the southward component
325 of the currents at the different stations. As expected from a depth-averaged
326 model, the best fit with observations is obtained at the shallowest mooring
327 C10, located on the 25 m isobath, with an average veering angle of 6° and
328 smaller error statistics (Table 1).

329 The simulated significant wave height agrees well with observations on
330 the WFS, where errors on the peak value do not exceed 5% (Fig. 8). On
331 Florida's eastern shelf, errors are slightly larger and reach 20%. Although the
332 model outputs agree well with observations, a lag in significant wave height is
333 observed for all 4 buoys. Moreover, the peak in significant wave height tends
334 to be underestimated at buoys 41113 and 41114, located on the eastern shelf
335 of Florida. The same tendency is observed with the modeled wave period,
336 with mean errors inferior to 1 second on the WFS and reaching more than
337 2 seconds on Florida's eastern shelf (Table 1), as the coupled model fails
338 to reproduce the observed peak in wave period between the 7th and 8th of

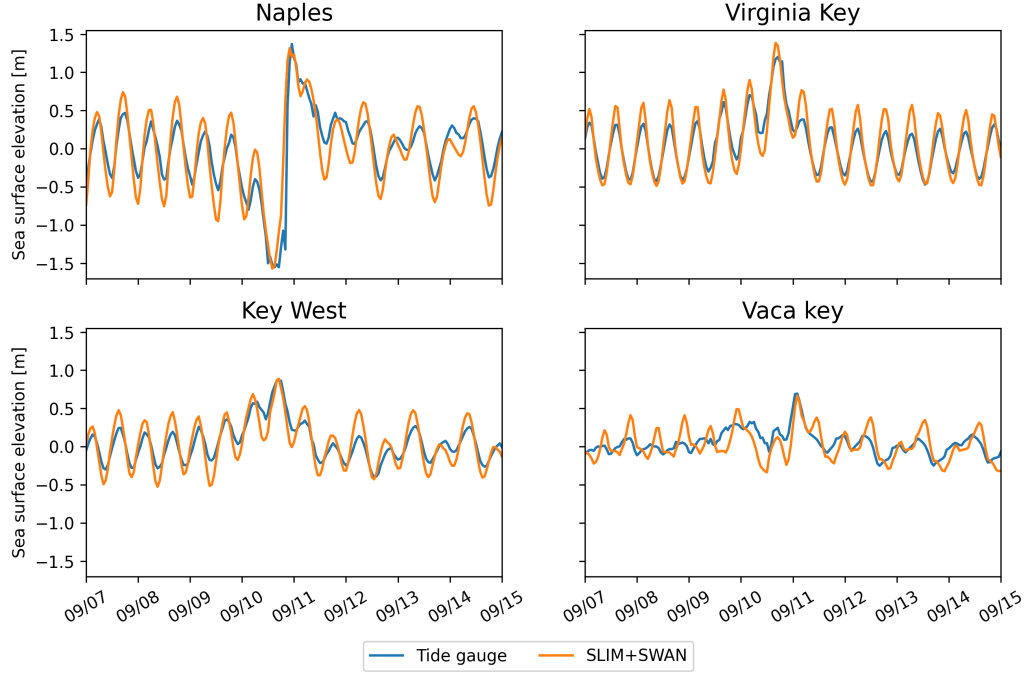


Fig. 6: Comparison of modeled sea surface elevation at the 4 tide gauges shown in Fig. 1B. The timing and amplitudes of the storm surges are well reproduced by the model

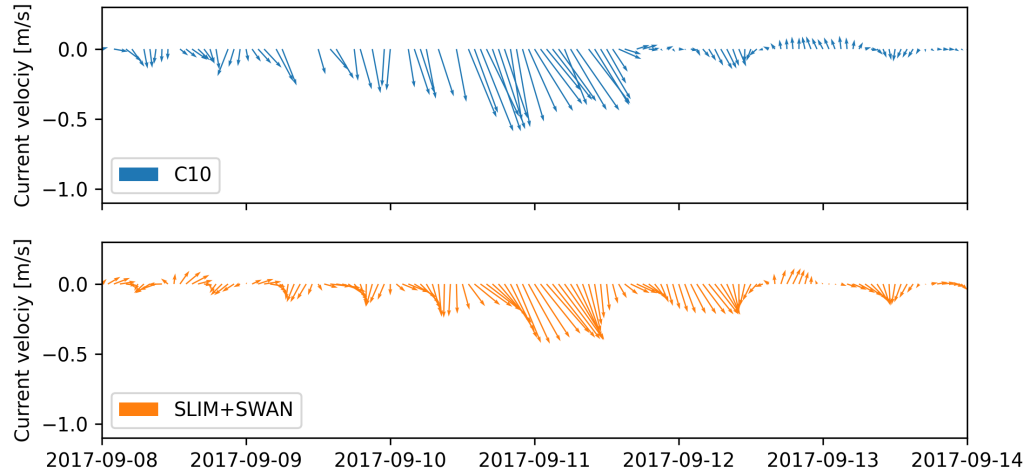


Fig. 7: Comparison of modeled current velocity with observed velocity at mooring C10 (see Fig. 1B for its location). modeled current velocities agree well with observations, with a correlation coefficient of 0.83 and an average veering angle of 6°.

339 September on this side of Florida. Finally, modeled wave direction agrees well
340 with observation (Fig. 8), although our model tends to overestimate wave
341 propagation in the northward direction at stations 41114 and 41113 on the
342 passage of the hurricane.

343 *3.2. Impact of waves on currents and transport*

344 We evaluated the impact of wave-current interactions on modeled currents
345 during the passage of Irma in the Lower Keys, between Sept. 7 and 13, 2017.
346 First, we computed the maximum difference between currents modeled by
347 SLIM and SLIM+SWAN during this period (Fig. 9A). The largest differences
348 in current speed were observed over the reefs, on the shelf break and around
349 islands. They can locally reach 1 m/s, with the coupled SLIM+SWAN model
350 yielding the largest amplitudes. The regions where the differences are the
351 largest experience the strongest radiation-stress gradient τ_{wave} (Fig. 9B)
352 induced by wave energy dissipation on the shelf-break and rough seabed
353 induce variations of the wave radiation stress (Longuet-Higgins and Stewart,
354 1964). This highlights the important protective role of the barrier formed
355 by the offshore reefs, that require a fine spatial resolution to be accurately
356 captured. Wave-induced differences in current speed were amplified by the
357 action of the wind stress τ_{wind} (Fig. 9C). Wind speeds were larger in the front
358 right quadrant of the hurricane (Zedler et al., 2009), yielding larger differences
359 on the right-hand side of the storm trajectory. This is especially clear in the
360 area between the Florida Keys and the Everglades, where relatively small
361 values of τ_{wave} nonetheless produce current speed differences of up to 0.5 m/s
362 because of the wind stress.

363 Waves play a significant role on the transport processes during and after the
364 passage of hurricane Irma (Fig. 10A,B). Comparing SLIM and SLIM+SWAN
365 shows that wave-current interactions alone yield differences of up to 5 km
366 between the modeled trajectories on the passage of the hurricane. These
367 differences exceed 10 km on the outer shelf when Stokes drift is taken into
368 account. The impact of the waves on the transport processes differs signifi-

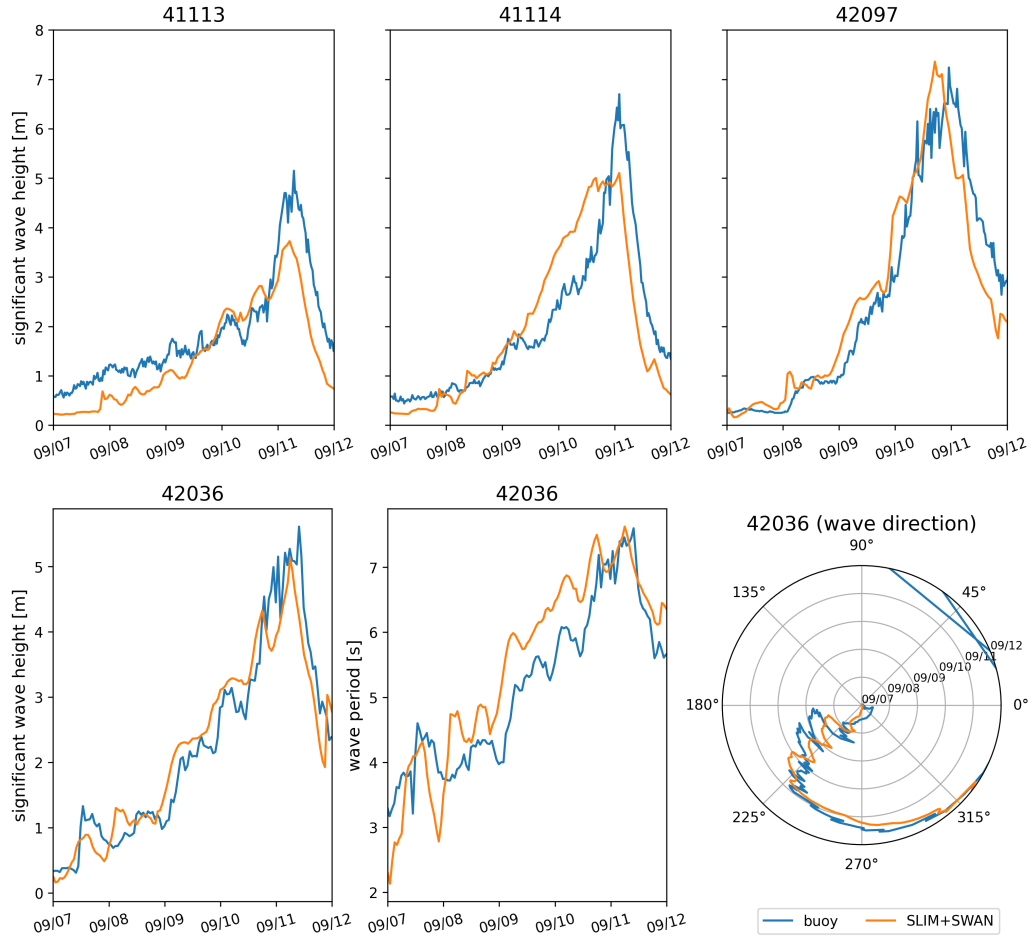


Fig. 8: Comparison of modeled wave parameters with observation at the 4 buoys location (locations shown in Fig. 1B). The modeled significant wave heights agree well with field measurement.

Station	Variable	Bias	MAE	RMSE
Vaca Key	sse (m)	n/a	0.12	0.16
	U_{10} (m/s)	1.51	1.85	2.61
	p_{atm} (hPa)	-0.21	0.59	1.03
Key West	sse (m)	n/a	0.11	0.13
Virginia Key	sse (m)	n/a	0.10	0.13
Naples	sse (m)	n/a	0.18	0.23
C10	u (m/s)	-0.006	0.04	0.05
	v (m/s)	0.02	0.06	0.08
C12	u (m/s)	-0.01	0.06	0.07
	v (m/s)	0.06	0.09	0.11
C13	u (m/s)	0.004	0.06	0.08
	v (m/s)	0.04	0.06	0.08
41113	H_s (m)	-0.35	0.40	0.51
	T_m (s)	-2.18	2.47	3.13
	θ_m (degree)	7.17	19.50	26.06
41114	H_s (m)	-0.21	0.53	0.68
	T_m (s)	-1.69	2.53	3.15
	θ_m (degree)	31.25	35.28	46.18
42036	H_s (m)	-0.03	0.26	0.36
	T_m (s)	0.04	0.65	0.77
	θ_m (degree)	19.92	30.65	41.69
42097	H_s (m)	-0.15	0.40	0.57
	T_m (s)	0.02	0.62	0.74
	θ_m (degree)	3.62	28.08	45.89

Table 1: Error statistics on the wave-current model outputs as compared to the measured sea surface elevation (sse), eastward and northward depth-average current velocities (u,v), significant wave height (H_s), zero-crossing mean wave period (T_m) and mean wave direction (θ_m). Model bias, mean absolute error (MAE), and root mean squared error (RMSE) are listed by variable (unit) and value.

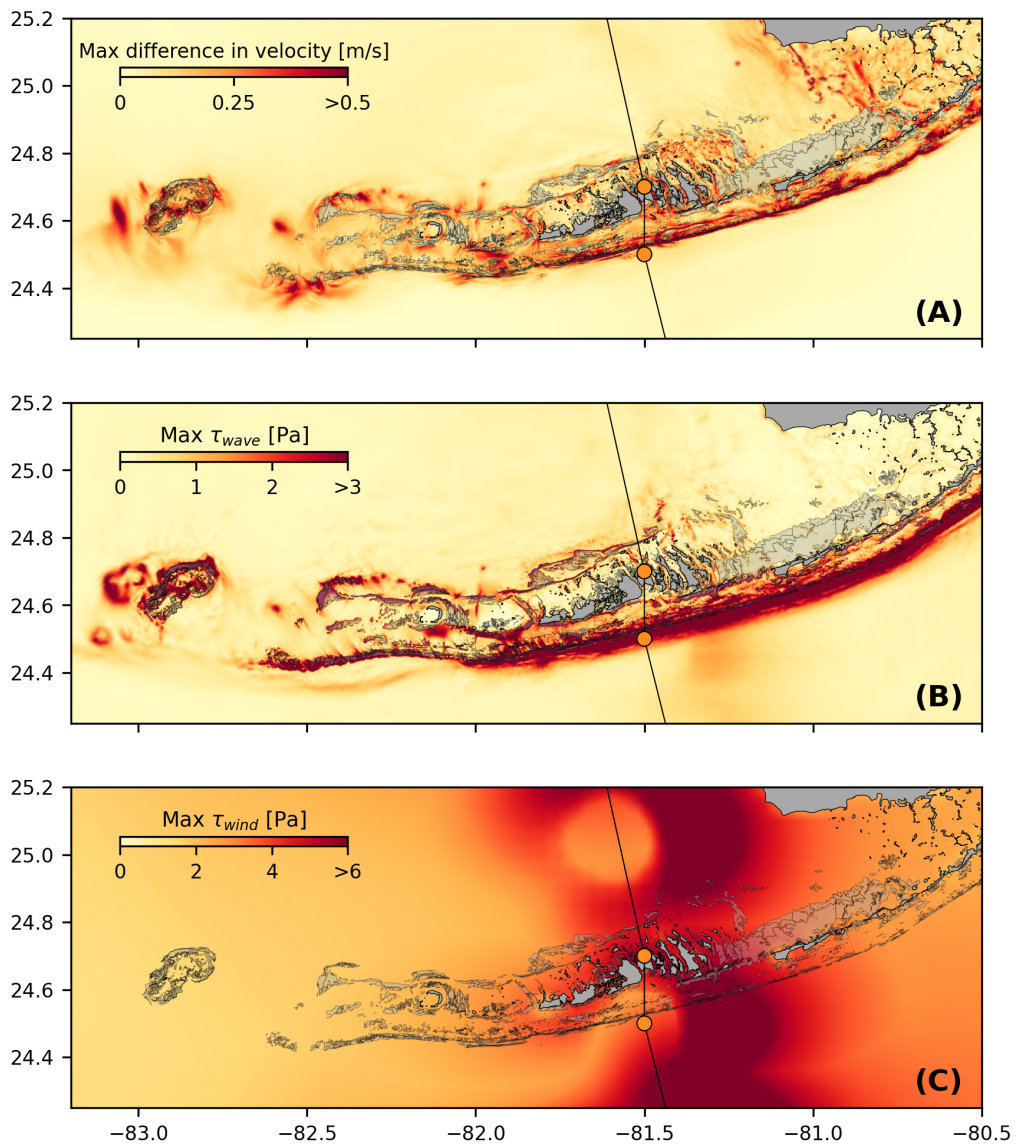


Fig. 9: (A). Maximum difference between SLIM and SLIM+SWAN currents during the passage of Irma in the Lower Florida Keys; (B) Maximum wave radiation stress gradient τ_{wave} and (C) maximum wind stress τ_{wind} (C) generated by the hurricane. Radiation stress gradient yields difference larger than 0.5 m/s (and locally reaching 1m/s) in current velocities, especially over offshore reefs.

369 cantly between the inner and outer shelves, with wave-induced differences in
370 trajectories 4 to 5 times larger on the outer shelf. Furthermore, the distance
371 between the centers of mass of the clouds of particles tends to stabilize on
372 the inner shelf after the passage of Irma, while it keeps increasing on the
373 other shelf up to two days after the passage of the hurricane when taking
374 Stokes drift into account. The distance then stabilizes for about a day before
375 it starts decreasing (see right panel of Fig. 10A,B). However, when consider-
376 ing wave-current interactions alone (SLIM vs. SLIM+SWAN), the distance
377 between the clouds of particles starts to decrease just after the passage of
378 Irma.

379 The Stokes drift appears to have a larger effect than the radiation stress
380 gradient and the wave-current interactions (Fig 10A,B). Nonetheless, compar-
381 ing the different curves for the outer shelf suggests that the radiation-stress
382 gradient induces effects similar to the impact of the Stokes drift in this
383 region during the passage of Irma. However, when comparing SLIM and
384 SLIM+SWAN both on the inner and other shelf, this impact appears to be
385 negligible during the rest of the simulation. Comparing Stokes-U and Stokes-C
386 indicates that the difference between the trajectories of particles advected by
387 the two Stokes drifts does not exceed 2 km, with larger discrepancies on the
388 outer shelf (Fig. 10C,D). The distance between the two clouds of particles
389 increases abruptly on the passage of the hurricane (and two days after on the
390 outer shelf) and then stabilizes during the rest of the simulation.

391 4. Discussion

392 The coupled SLIM+SWAN model correctly reproduces the hydrodynamics
393 and wave dynamics during hurricane Irma. Such good agreement with field
394 measurements can only be achieved using accurate forcings and adequate
395 wave parameterizations. By comparing coupled and uncoupled model runs, we
396 showed that neglecting wave radiation stress gradient can induce differences
397 of up to 1 m/s in modeled current velocities. The radiation stress gradient

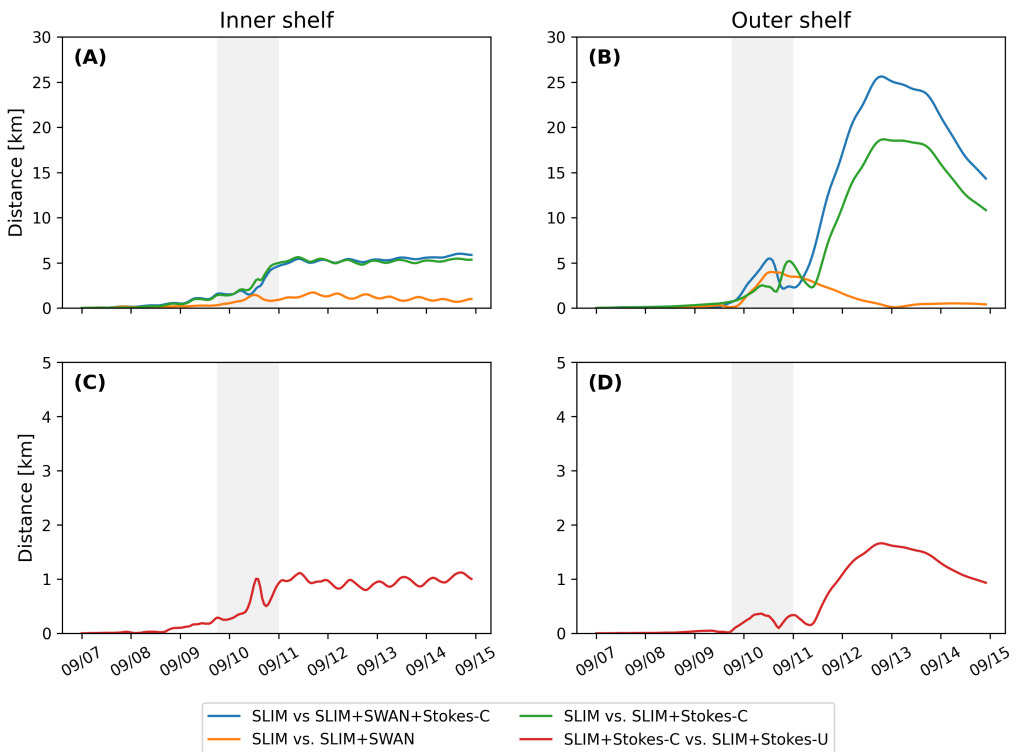


Fig. 10: Difference between the centers of mass of the particle clouds released from the regions highlighted in Fig. 4 and advected by different combinations of coupled and uncoupled velocity fields.

398 during the hurricane was especially large over the shelf break, where waves
399 are strongly dissipated by the offshore coral reef barrier. The radiation stress
400 gradient alone can deflect drifting particles by up to 5 km during the passage
401 of the hurricane. These differences in modeled trajectories were significantly
402 larger and required more time to stabilize on the outer shelf. The impact of
403 the Stokes drift dominates the effects of wave-current interactions through the
404 radiation stress gradient, except during the passage of the hurricane, when
405 both contributions are similar. Finally, neglecting wave-current interactions
406 when computing Stokes drift leads to variations of up to 2 km in modeled
407 trajectories on the passage of the hurricane.

408 Despite slightly overestimating the amplitude of the sea surface elevation in
409 fair weather conditions, the coupled wave-current model correctly reproduces
410 the timing and amplitude of the observed storm surge. All elevation peaks are
411 captured with a 4% accuracy at every stations except Virginia key, where the
412 surge was overestimated by about 15%. Such accuracy is key to predict the
413 damages caused by the hurricane, as most destroyed and severely damaged
414 buildings in the Florida Keys during Hurricane Irma were caused by storm
415 surge and waves (Xian et al., 2018). Furthermore, by using a high-resolution
416 model, we can explicitly reproduce the circulation between all the reefs and
417 islands of the Florida Keys. The fine-scale details of the storm surge, and
418 hence the associated risk, are thus accurately represented. In addition to
419 accurately capturing positive surges, the model also reproduced the observed
420 negative surge in Naples with an error of about 1%. This result is of interest
421 from a biological point of view as negative surges, although less studied, affect
422 water exchanges between the estuaries and the coastal ocean and disturb
423 the benthic ecosystems (Liu et al., 2020). Such rapid decrease in water level
424 followed by a positive surge cause massive freshwater inflows, generating a
425 significant decrease in water salinity (Wachnicka et al., 2019).

426 Strong currents such as the Gulf Stream affect waves trough refraction
427 over gradients in current velocity, shoaling and breaking of opposing waves or

lengthening of following waves (Hegermiller et al., 2019). Under hurricane conditions, these interactions can cause numerical instabilities in the wave model if the parameterizations are not appropriate and the model resolution not sufficient. Hegermiller et al. (2019), for instance, used a 5-km model grid and 48 directional bins to capture spatial gradients in wave height induced by wave-currents interactions in the Gulf Stream during Hurricane Matthew (2016). We followed these guidelines when defining the coarsest resolution of the model mesh as well as the spectral discretization of SWAN. Boundary conditions and directional spreading of the incident waves also play a significant role when modeling wave-current interactions at meso- and submesoscales (Villas Bôas et al., 2020), which motivated our choice of imposing full spectra on the boundary of the wave model instead of bulk parameters. Finally, SWAN default parameterizations for wind energy input and whitecapping caused numerical instabilities by overestimating wave growth and steepness on the boundary of the Gulf Stream on the passage of Irma. This overestimation was solved by using the parameterization of Siadatmousavi et al. (2011). The parameters used in this study were calibrated on the Northern Gulf of Mexico, which might explains that our model better reproduces wave parameters at buoys located on the WFS. However, these calibrated parameters might underestimate wind-induced wave growth on Florida's eastern shelf. Consequently, incident wave do not receive enough energy to grow after breaking on the bank boundary, leading to an underestimation of the significant wave height at buoys located on Florida's eastern shelf. A more extensive calibration study might therefore be necessary to further improve the agreement with field measurements on both sides of Florida. Nonetheless, as this study focuses on the wave produced by Irma, which made landfall on the western coasts of Florida, the use of parameterizations calibrated for the Gulf of Mexico seems reasonable.

The radiation stress gradient significantly impacts currents during the passage of the hurricane. It can induce differences of up to 1 m/s in the

458 current speed on the shelf break. In this region waves are strongly dissipated
459 due to action of depth-induced breaking and bottom dissipation on coral reefs.
460 This highlights the protective role of coral reefs against strong incoming waves
461 (Lowe et al., 2005), which requires a sufficiently fine spatial resolution to be
462 explicitly represented in the model. Due to the dissipation of incoming waves
463 on the reefs, wave impact during Irma is different on the inner and outer
464 shelves. It is less important on the inner shelf because of the sheltering of the
465 inner shelf due to reefs and islands as well as wave breaking on the shelf break.
466 The inner shelf hence experiences weaker waves and currents, inducing weaker
467 and more localized transport. Furthermore, the impact of winds on waves
468 is reduced in shallower areas under the action of depth-induced breaking.
469 This might explain why differences between particle trajectories stabilize
470 on the inner shelf just after the passage of Hurricane Irma. However, the
471 Florida Keys still experienced strong winds after the passage of the core of the
472 hurricane, which generated high waves in the deeper areas. This might explain
473 why the differences on between the modeled trajectories kept increasing on
474 the outer shelf under the action of strong Stokes drift up to two days after
475 the passage of the hurricane.

476 The distance between the centers of mass of the particle clouds advected
477 by coupled and uncoupled Stokes drift remains rather limited (< 2 km). This
478 suggest that taking wave-currents interactions into account when computing
479 Stokes drift, even in heavy wind conditions has a limited impact. Furthermore,
480 combining the coupled Stokes drift with the coupled and uncoupled SLIM
481 currents produced similar trajectories on the inner shelf, which seems to
482 indicate that wave impact on currents is limited in this region. This would
483 suggest that it is not necessary to take wave-current interactions into account
484 when modeling the trajectories of tracers in shallow, sheltered areas such
485 as the inner WFS during a hurricane. Uncoupled currents with uncoupled
486 Stokes drift should give a reasonably accurate approximation of the transport
487 processes. However, this does not hold for deeper and unsheltered regions,

488 as highlighted by the comparison of trajectories obtained with coupled and
489 uncoupled SLIM currents combined with coupled Stokes drift on the outer
490 shelf.

491 **5. Conclusion**

492 We developed a coupled wave-current model to study the impact of
493 waves on transport processes during Hurricane Irma. In order to accurately
494 represent the wind and pressure profiles of te hurricane, we built hybrid fields
495 by combining coarser ERA-5 data with high-resolution H*Wind data for
496 the wind speed and idealized Holland profiles for the pressure. Comparing
497 these hybrid profiles with field observations showed that they were better at
498 reproducing the observed central depression of the hurricane as well as the
499 peak in wind speed than ERA-5 data. Using these hybrid fields as forcings,
500 our coupled model accurately reproduced the storm surge at NDBC buoy
501 locations and produced currents and wave parameters in good agreement
502 with field observations, especially on the WFS. The modeled currents and
503 Stokes drift were then used to evaluate the impact of waves on the trajectory
504 of passive drifters on the passage of the hurricane through the Florida Keys.
505 Our results show that waves had a significant impact on heavy-wind transport
506 processes and caused deflections of the drifters trajectories by more than 20
507 km on the outer shelf.

508 Despite its good agreement with observations, our model could be fur-
509 ther refined by improving the representation of wind-wave interactions. In
510 particular, it does not consider the momentum loss due to the action of
511 surface waves when representing momentum flux from the atmosphere to the
512 ocean, leading to overestimations under hurricane conditions. Our model
513 could therefore be further improved by using wave-dissipative stress instead
514 of the full wind stress as the momentum flux from the atmosphere to the
515 ocean. Moreover, a more thorough calibration of the wave model parameters
516 should improve our model results on Florida's eastern shelf. Finally, as a 2D

517 barotropic model, SLIM does not explicitly represent baroclinic phenomena
518 as well as the vertical profile of the Stokes drift and radiation stress gradient
519 along the wave boundary layer. However, our study focused on relatively
520 shallow and vertically homogeneous coastal waters using a reef-scale resolution
521 throughout the whole FRT. Such fine resolution allows to explicitly represent
522 wave dissipation over coral reefs and is only achievable using a 2D model due
523 to computational resources limitations.

524 Wave coupling needs to be taken into account during heavy-wind events
525 but not necessarily in milder conditions. While the radiation stress gradient
526 plays an important role and can lead to differences of up to 5 km, the
527 Stokes drift is about 4 times more intense and should thus be considered
528 in priority. This study brings new insight on the impact of waves on the
529 transport processes nearshore during a tropical cyclone. Due to its high
530 spatial resolution, the developed coupled wave-current model can be used
531 to accurately represent the dispersal of pollutants, sediments or larvae in
532 topologically complex coastal areas in heavy-wind conditions.

533 Acknowledgments

534 Computational resources were provided by the Consortium des Équipements
535 de Calcul Intensif (CÉCI), funded by the F.R.S.-FNRS under Grant No.
536 2.5020.11. Thomas Dobbelaere is a PhD student supported by the Fund for
537 Research training in Industry and Agriculture (FRIA/FNRS).

538 References

- 539 Benoit, M., Marcos, F., Becq, F., 1997. TOMAWAC: A prediction model for
540 offshore and nearshore storm waves. Environmental and Coastal Hydraulics:
541 Protecting the Aquatic Habitat, Proceedings of Theme B 1 & 2, 1316–1321.
- 542 Bever, A.J., MacWilliams, M.L., 2013. Simulating sediment transport pro-
543 cesses in San Pablo Bay using coupled hydrodynamic, wave, and sediment
544 transport models. Marine Geology 345, 235–253.

- 545 Bhatia, K.T., Vecchi, G.A., Knutson, T.R., Murakami, H., Kossin, J., Dixon,
546 K.W., Whitlock, C.E., 2019. Recent increases in tropical cyclone intensifi-
547 cation rates. *Nature Communications* 10, 1–9.
- 548 Booij, N., Ris, R.C., Holthuijsen, L.H., 1999. A third-generation wave
549 model for coastal regions: 1. Model description and validation. *Journal of*
550 *Geophysical Research: Oceans* 104, 7649–7666.
- 551 Breivik, Ø., Allen, A.A., Maisondieu, C., Olagnon, M., 2013. Advances in
552 search and rescue at sea. *Ocean Dynamics* 63, 83–88.
- 553 Chassignet, E.P., Hurlburt, H.E., Smedstad, O.M., Halliwell, G.R., Hogan,
554 P.J., Wallcraft, A.J., Baraille, R., Bleck, R., 2007. The HYCOM (hybrid
555 coordinate ocean model) data assimilative system. *Journal of Marine*
556 *Systems* 65, 60–83.
- 557 Craik, A.D., Leibovich, S., 1976. A rational model for Langmuir circulations.
558 *Journal of Fluid Mechanics* 73, 401–426.
- 559 Curcic, M., 2015. Explicit air-sea momentum exchange in coupled atmosphere-
560 wave-ocean modeling of tropical cyclones. Ph.D. thesis. University of Miami.
- 561 Curcic, M., Chen, S.S., Özgökmen, T.M., 2016. Hurricane-induced ocean
562 waves and stokes drift and their impacts on surface transport and dispersion
563 in the Gulf of Mexico. *Geophysical Research Letters* 43, 2773–2781.
- 564 Curcic, M., Haus, B.K., 2020. Revised estimates of ocean surface drag in
565 strong winds. *Geophysical Research Letters* 47, e2020GL087647.
- 566 Dietrich, J., Bunya, S., Westerink, J., Ebersole, B., Smith, J., Atkinson,
567 J., Jensen, R., Resio, D., Luettich, R., Dawson, C., et al., 2010. A high-
568 resolution coupled riverine flow, tide, wind, wind wave, and storm surge
569 model for southern Louisiana and Mississippi. Part II: Synoptic description
570 and analysis of Hurricanes Katrina and Rita. *Monthly Weather Review*
571 138, 378–404.

- 572 Dietrich, J., Westerink, J., Kennedy, A., Smith, J., Jensen, R., Zijlema, M.,
573 Holthuijsen, L., Dawson, C., Luettich, R., Powell, M., et al., 2011. Hurricane
574 Gustav (2008) waves and storm surge: Hindcast, synoptic analysis, and
575 validation in southern Louisiana. *Monthly Weather Review* 139, 2488–2522.
- 576 Dietrich, J.C., Tanaka, S., Westerink, J.J., Dawson, C., Luettich, R., Zijlema,
577 M., Holthuijsen, L.H., Smith, J., Westerink, L., Westerink, H., 2012. Per-
578 formance of the unstructured-mesh, SWAN+ ADCIRC model in computing
579 hurricane waves and surge. *Journal of Scientific Computing* 52, 468–497.
- 580 Dobbelaere, T., Muller, E.M., Gramer, L.J., Holstein, D.M., Hanert, E., 2020.
581 Coupled epidemic-hydrodynamic modeling to understand the spread of a
582 deadly coral disease in Florida. *Frontiers in Marine Science* 7, 1016.
- 583 Donelan, M., Haus, B., Reul, N., Plant, W., Stiassnie, M., Graber, H., Brown,
584 O., Saltzman, E., 2004. On the limiting aerodynamic roughness of the
585 ocean in very strong winds. *Geophysical Research Letters* 31.
- 586 Drivdal, M., Broström, G., Christensen, K., 2014. Wave-induced mixing and
587 transport of buoyant particles: Application to the Statfjord A oil spill.
588 *Ocean Science* 10, 977–991.
- 589 Figueiredo, J., Baird, A.H., Connolly, S.R., 2013. Synthesizing larval com-
590 petence dynamics and reef-scale retention reveals a high potential for
591 self-recruitment in corals. *Ecology* 94, 650–659.
- 592 Fringer, O.B., Dawson, C.N., He, R., Ralston, D.K., Zhang, Y.J., 2019. The
593 future of coastal and estuarine modeling: Findings from a workshop. *Ocean
594 Modelling* 143, 101458.
- 595 Frys, C., Saint-Amand, A., Le Hénaff, M., Figueiredo, J., Kuba, A., Walker,
596 B., Lambrechts, J., Vallaey, V., Vincent, D., Hanert, E., 2020. Fine-scale
597 coral connectivity pathways in the Florida Reef Tract: Implications for
598 conservation and restoration. *Frontiers in Marine Science* 7, 312.

- 599 Geuzaine, C., Remacle, J.F., 2009. Gmsh: A 3-d finite element mesh generator
600 with built-in pre-and post-processing facilities. International journal for
601 numerical methods in engineering 79, 1309–1331.
- 602 Harper, B., Kepert, J., Ginger, J., 2010. Guidelines for converting between
603 various wind averaging periods in tropical cyclone conditions.
- 604 Hegermiller, C.A., Warner, J.C., Olabarrieta, M., Sherwood, C.R., 2019.
605 Wave-current interaction between Hurricane Matthew wave fields and the
606 Gulf Stream. Journal of Physical Oceanography 49, 2883–2900.
- 607 Hoefel, F., Elgar, S., 2003. Wave-induced sediment transport and sandbar
608 migration. Science 299, 1885–1887.
- 609 Holthuijsen, L.H., Powell, M.D., Pietrzak, J.D., 2012. Wind and waves in
610 extreme hurricanes. Journal of Geophysical Research: Oceans 117.
- 611 Janssen, P.A., 1991. Quasi-linear theory of wind-wave generation applied to
612 wave forecasting. Journal of Physical Oceanography 21, 1631–1642.
- 613 Johns, W.E., Schott, F., 1987. Meandering and transport variations of the
614 Florida Current. Journal of Physical Oceanography 17, 1128–1147.
- 615 Knaff, J.A., Sampson, C.R., Musgrave, K.D., 2018. Statistical tropical cyclone
616 wind radii prediction using climatology and persistence: Updates for the
617 western North Pacific. Weather and Forecasting 33, 1093–1098.
- 618 Knutson, T., Camargo, S.J., Chan, J.C., Emanuel, K., Ho, C.H., Kossin, J.,
619 Mohapatra, M., Satoh, M., Sugi, M., Walsh, K., et al., 2020. Tropical
620 cyclones and climate change assessment: Part II: Projected response to
621 anthropogenic warming. Bulletin of the American Meteorological Society
622 101, E303–E322.

- 623 Komen, G., Hasselmann, S., Hasselmann, K., 1984. On the existence of a
624 fully developed wind-sea spectrum. *Journal of Physical Oceanography* 14,
625 1271–1285.
- 626 Kossin, J.P., Knapp, K.R., Olander, T.L., Velden, C.S., 2020. Global increase
627 in major tropical cyclone exceedance probability over the past four decades.
628 *Proceedings of the National Academy of Sciences* 117, 11975–11980.
- 629 Kourafalou, V.H., Kang, H., 2012. Florida Current meandering and evo-
630 lution of cyclonic eddies along the Florida Keys Reef Tract: Are they
631 interconnected? *Journal of Geophysical Research: Oceans* 117.
- 632 Kundu, P.K., 1976. Ekman veering observed near the ocean bottom. *Journal*
633 *of Physical Oceanography* 6, 238–242.
- 634 Lambrechts, J., Hanert, E., Deleersnijder, E., Bernard, P.E., Legat, V.,
635 Remacle, J.F., Wolanski, E., 2008. A multi-scale model of the hydrodynam-
636 ics of the whole Great Barrier Reef. *Estuarine, Coastal and Shelf Science*
637 79, 143–151.
- 638 Landsea, C.W., Franklin, J.L., 2013. Atlantic hurricane database uncertainty
639 and presentation of a new database format. *Monthly Weather Review* 141,
640 3576–3592.
- 641 Lane, E.M., Restrepo, J., McWilliams, J.C., 2007. Wave-current interaction:
642 A comparison of radiation-stress and vortex-force representations. *Journal*
643 *of Physical Oceanography* 37, 1122–1141.
- 644 Langmuir, I., 1938. Surface motion of water induced by wind. *Science* 87,
645 119–123.
- 646 Le, H.A., Lambrechts, J., Ortaleb, S., Gratiot, N., Deleersnijder, E., Soares-
647 Frazão, S., 2020. An implicit wetting–drying algorithm for the discontinuous
648 galerkin method: application to the tonle sap, mekong river basin. *Envi-
649 ronmental Fluid Mechanics* , 1–29.

- 650 Le Hénaff, M., Kourafalou, V.H., Paris, C.B., Helgers, J., Aman, Z.M., Hogan,
651 P.J., Srinivasan, A., 2012. Surface evolution of the Deepwater Horizon
652 oil spill patch: Combined effects of circulation and wind-induced drift.
653 Environmental Science & Technology 46, 7267–7273.
- 654 Lee, T.N., Leaman, K., Williams, E., Berger, T., Atkinson, L., 1995. Florida
655 Current meanders and gyre formation in the southern Straits of Florida.
656 Journal of Geophysical Research: Oceans 100, 8607–8620.
- 657 Lee, T.N., Mayer, D.A., 1977. Low-frequency current variability and spin-off
658 eddies along the shelf off southeast Florida. Collected Reprints 1, 344.
- 659 Lee, T.N., Smith, N., 2002. Volume transport variability through the Florida
660 Keys tidal channels. Continental Shelf Research 22, 1361–1377.
- 661 Lee, T.N., Williams, E., 1988. Wind-forced transport fluctuations of the
662 Florida Current. Journal of Physical Oceanography 18, 937–946.
- 663 Li, Z., Johns, B., 1998. A three-dimensional numerical model of surface
664 waves in the surf zone and longshore current generation over a plane beach.
665 Estuarine, Coastal and Shelf Science 47, 395–413.
- 666 Lin, N., Chavas, D., 2012. On hurricane parametric wind and applications in
667 storm surge modeling. Journal of Geophysical Research: Atmospheres 117.
- 668 Liu, Y., Weisberg, R.H., 2012. Seasonal variability on the West Florida shelf.
669 Progress in Oceanography 104, 80–98.
- 670 Liu, Y., Weisberg, R.H., Zheng, L., 2020. Impacts of hurricane Irma on the
671 circulation and transport in Florida Bay and the Charlotte Harbor estuary.
672 Estuaries and Coasts 43, 1194–1216.
- 673 Liubartseva, S., Coppini, G., Lecci, R., Clementi, E., 2018. Tracking plastics
674 in the Mediterranean: 2D Lagrangian model. Marine Pollution Bulletin
675 129, 151–162.

- 676 Longuet-Higgins, M.S., 1970. Longshore currents generated by obliquely
677 incident sea waves. *Journal of Geophysical Research* 75, 6778–6789.
- 678 Longuet-Higgins, M.S., Stewart, R., 1964. Radiation stresses in water waves;
679 a physical discussion, with applications, in: *Deep Sea Research and Oceanographic Abstracts*, Elsevier. pp. 529–562.
- 681 Lowe, R.J., Falter, J.L., Bandet, M.D., Pawlak, G., Atkinson, M.J., Moni-
682 smith, S.G., Koseff, J.R., 2005. Spectral wave dissipation over a barrier
683 reef. *Journal of Geophysical Research: Oceans* 110.
- 684 Madsen, O.S., Poon, Y.K., Gruber, H.C., 1989. Spectral wave attenuation by
685 bottom friction: Theory, in: *Coastal Engineering 1988*, pp. 492–504.
- 686 Malmstadt, J., Scheitlin, K., Elsner, J., 2009. Florida hurricanes and damage
687 costs. *Southeastern Geographer* 49, 108–131.
- 688 McWilliams, J.C., Restrepo, J.M., Lane, E.M., 2004. An asymptotic theory
689 for the interaction of waves and currents in coastal waters. *Journal of Fluid
690 Mechanics* 511, 135.
- 691 McWilliams, J.C., Sullivan, P.P., 2000. Vertical mixing by Langmuir circula-
692 tions. *Spill Science & Technology Bulletin* 6, 225–237.
- 693 Mei, C.C., 1989. The applied dynamics of ocean surface waves. volume 1.
694 World scientific.
- 695 Moon, I.J., Ginis, I., Hara, T., Thomas, B., 2007. A physics-based parame-
696 terization of air-sea momentum flux at high wind speeds and its impact on
697 hurricane intensity predictions. *Monthly Weather Review* 135, 2869–2878.
- 698 Pinelli, J.P., Roueche, D., Kijewski-Correa, T., Plaz, F., Prevatt, D., Zisis,
699 I., Elawady, A., Haan, F., Pei, S., Gurley, K., et al., 2018. Overview of
700 damage observed in regional construction during the passage of Hurricane
701 Irma over the State of Florida, in: *Forensic Engineering 2018: Forging*

- 702 Forensic Frontiers. American Society of Civil Engineers Reston, VA, pp.
703 1028–1038.
- 704 Powell, M.D., Houston, S.H., Amat, L.R., Morisseau-Leroy, N., 1998. The
705 HRD real-time hurricane wind analysis system. Journal of Wind Engineering
706 and Industrial Aerodynamics 77, 53–64.
- 707 Powell, M.D., Vickery, P.J., Reinhold, T.A., 2003. Reduced drag coefficient
708 for high wind speeds in tropical cyclones. Nature 422, 279–283.
- 709 Röhrs, J., Christensen, K.H., Hole, L.R., Broström, G., Drivdal, M., Sundby,
710 S., 2012. Observation-based evaluation of surface wave effects on currents
711 and trajectory forecasts. Ocean Dynamics 62, 1519–1533.
- 712 Schott, F.A., Lee, T.N., Zantopp, R., 1988. Variability of structure and
713 transport of the Florida Current in the period range of days to seasonal.
714 Journal of Physical Oceanography 18, 1209–1230.
- 715 Siadatmousavi, S.M., Jose, F., Stone, G., 2011. Evaluation of two WAM
716 white capping parameterizations using parallel unstructured SWAN with
717 application to the Northern Gulf of Mexico, USA. Applied Ocean Research
718 33, 23–30.
- 719 Sikirić, M.D., Roland, A., Janečković, I., Tomazić, I., Kuzmić, M., 2013.
720 Coupling of the Regional Ocean Modeling System (ROMS) and Wind
721 Wave Model. Ocean Modelling 72, 59–73.
- 722 Smith, N.P., 1982. Response of Florida Atlantic shelf waters to hurricane
723 David. Journal of Geophysical Research: Oceans 87, 2007–2016.
- 724 Spivakovskaya, D., Heemink, A., Milstein, G., Schoenmakers, J., 2005. Sim-
725 ulation of the transport of particles in coastal waters using forward and
726 reverse time diffusion. Advances in water resources 28, 927–938.

- 727 Stokes, G.G., 1880. On the theory of oscillatory waves. *Transactions of the*
728 *Cambridge Philosophical Society* .
- 729 Tolman, H.L., et al., 2009. User manual and system documentation of
730 WAVEWATCH III TM version 3.14. Technical note, MMAB Contribution
731 276, 220.
- 732 Van Den Bremer, T., Breivik, Ø., 2018. Stokes drift. *Philosophical Trans-*
733 *actions of the Royal Society A: Mathematical, Physical and Engineering*
734 *Sciences* 376, 20170104.
- 735 Villas Bôas, A.B., Cornuelle, B.D., Mazloff, M.R., Gille, S.T., Arduin, F.,
736 2020. Wave–current interactions at meso-and submesoscales: Insights from
737 idealized numerical simulations. *Journal of Physical Oceanography* 50,
738 3483–3500.
- 739 Wachnicka, A., Browder, J., Jackson, T., Louda, W., Kelble, C., Abdelrahman,
740 O., Stabenau, E., Avila, C., 2019. Hurricane Irmas impact on water quality
741 and phytoplankton communities in Biscayne Bay (Florida, USA). *Estuaries*
742 and Coasts , 1–18.
- 743 WAMDI Group, 1988. The WAM model – A third generation ocean wave
744 prediction model. *Journal of Physical Oceanography* 18, 1775–1810.
- 745 Weisberg, R., Liu, Y., Mayer, D., 2009. Mean circulation on the west Florida
746 continental shelf observed with long-term moorings. *Geophys. Res. Lett*
747 36, L19610.
- 748 Weisberg, R.H., Zheng, L., 2006. Hurricane storm surge simulations for
749 Tampa Bay. *Estuaries and Coasts* 29, 899–913.
- 750 Wu, L., Chen, C., Guo, P., Shi, M., Qi, J., Ge, J., 2011. A FVCOM-
751 based unstructured grid wave, current, sediment transport model, I. Model
752 description and validation. *Journal of Ocean University of China* 10, 1–8.

- 753 Xian, S., Feng, K., Lin, N., Marsooli, R., Chavas, D., Chen, J., Hatzikyriakou,
754 A., 2018. Brief communication: Rapid assessment of damaged residential
755 buildings in the Florida Keys after Hurricane Irma. *Natural Hazards and*
756 *Earth System Sciences* 18, 2041–2045.
- 757 Zedler, S., Niiler, P., Stammer, D., Terrill, E., Morzel, J., 2009. Ocean's
758 response to Hurricane Frances and its implications for drag coefficient
759 parameterization at high wind speeds. *Journal of Geophysical Research: Oceans* 114.
- 760
761 Zhang, C., Durgan, S.D., Lagomasino, D., 2019. Modeling risk of mangroves
762 to tropical cyclones: A case study of Hurricane Irma. *Estuarine, Coastal and Shelf Science* 224, 108–116.
763